This is the accepted manuscript made available via CHORUS. The article has been published as:

Correlated spin-flip tunneling in a Fermi lattice gas

Wenchao Xu, William Morong, Hoi-Yin Hui, Vito W. Scarola, and Brian DeMarco

Phys. Rev. A **98**, 023623 — Published 20 August 2018

DOI: 10.1103/PhysRevA.98.023623

Correlated Spin-Flip Tunneling in a Fermi Lattice Gas

Wenchao Xu,[1,*] William Morong,[1] Hoi-Yin Hui,[2] Vito W. Scarola,[2] and Brian DeMarco[1,†]

[1] *Department of Physics, University of Illinois at Urbana-Champaign, Urbana, Illinois 61801, USA*
[2] *Department of Physics, Virginia Tech, Blacksburg, Virginia 24061, USA*

(Dated: July 30, 2018)

We report the realization of correlated, density-dependent tunneling for fermionic ^{40}K atoms trapped in an optical lattice. By appropriately tuning the frequency difference between a pair of Raman beams applied to a spin-polarized gas, simultaneous spin transitions and tunneling events are induced that depend on the relative occupations of neighboring lattice sites. This correlated spin-flip tunneling (CSFT) is spectroscopically resolved using gases prepared in opposite spin states, and the inferred Hubbard interaction energy is compared with a tight-binding prediction. We measure the doublons created by the laser-induced correlated tunneling process using loss induced by light-assisted collisions. Furthermore, by controllably introducing vacancies to a spin-polarized gas, we demonstrate that correlated tunneling is suppressed when neighboring lattice sites are unoccupied. We explain how the CSFT quench implemented here prepares and evolves a large number of resonating-valence-bond (RVB) singlets in a Hubbard model, thus allowing exploration of RVB dynamics.

I. INTRODUCTION

Measurements on ultracold atoms trapped in optical lattices have emerged as a powerful approach to studying quantum phase transitions and dynamics in strongly correlated systems. Periodic driving forces and light-induced tunneling combined with optical lattices have enabled experiments to achieve physics beyond the minimal Hubbard model (see Ref. 1 for a recent review). For example, magnetic phase transitions have been probed [2, 3], synthetic gauge fields realized [4–7], and non-trivial band structures [8] have been created using periodic driving and external fields in lattices.

In this work, we use applied laser fields to demonstrate and study the dynamics of correlated tunneling that depends on density and spin for fermionic atoms. Correlated tunneling, known in solids as a bond-charge interaction, has been proposed to play a role in high-temperature superconductivity [9] and lattice stiffening in polyacetylene [10, 11]. The influence of correlated tunneling on transport properties has also been intensively investigated in quantum dots, where it can be manipulated by gate voltages and applied electromagnetic fields [12]. Beyond mimicking these effects in optical lattices, correlated tunneling for ultracold atoms has attracted theoretical interest for inducing occupation-dependent gauge fields [13], obtaining novel phases such as holon and doublon superfluids [14], and realizing anyonic Hubbard models [15]. Thus far, two-body correlated tunneling has been realized in double wells for bosons [16, 17] and fermions [18]. However, many-body density dependent tunneling has been directly observed only for bosonic atoms trapped in optical lattices [19, 20].

Inspired by the theoretical proposals in Ref. 21, we implement a new experimental approach to generate spin and density-dependent tunneling for fermionic atoms. This technique is fundamentally different from those already used to realize inter-site interactions in two key ways. First, prior approaches [16–20, 22] conserve spin, whereas the spin-flips induced via our method can lead to more exotic physics. Second, the inter-site interaction generated in our work is between fermionic atoms and spans the entire lattice, which leads to challenging many-body physics due to the fermion sign problem [23]. Our method is therefore able to prepare quantum many-body steady and excited states beyond the scope of previous experiments and exceeding the capabilities of current unbiased numerical modeling tools in two and three spatial dimensions. Specifically, we show that CSFT effectively creates singlet pairs to dynamically build RVB correlations [24, 25] in a Hubbard model. Prior work created RVB-singlets in four-site plaquettes in an optical superlattice [26]. Here we demonstrate a method to build up RVB correlations in large numbers of singlet pairs, which can be used to explore the many-body RVB states proposed by Anderson in the context of lattice models of high-temperature superconductivity.

To implement spin and density-dependent tunneling, we apply a pair of Raman beams to a spin-polarized gas, for which conventional tunneling is forbidden by the Pauli exclusion principle. The Raman beams flip the atomic spins and induce density-dependent tunneling. We spectroscopically resolve these CSFT events, and the corresponding increase in doubly occupied sites is measured using loss from light-assisted collisions. Moreover, by varying the filling fraction in the lattice, we directly verify the density-dependence of spin transitions.

The paper is organized as follows: In Section II we discuss the experimental setup used to observe CSFT. In Section III we discuss modeling of CSFT in the leading order dynamics. In Section IV we present measurements of spin transfer fraction and double occupancy to observe

* now at:Department of Physics, Massachusetts Institute of Technology, 77 Massachusetts Ave, Cambridge, MA 021139, USA
† bdemarco@illinois.edu

CSFT, and we summarize and discuss potential improvements to the experiment in Section V.

II. EXPERIMENTAL SETUP

These measurements are performed using a degenerate Fermi gas composed of ^{40}K atoms trapped in a cubic optical lattice in a regime described by a single-band Fermi-Hubbard model with tunneling energy t and interaction energy U (see Appendix A for details of the experimental sequence). We work in the $U/t \gtrsim 12$ regime, for which the ground state of a spin-mixed trapped gas possesses a Mott-insulator core [27]. Overall confinement is provided by a 1064 nm optical dipole trap. After cooling the gas in the dipole trap and before slowly superimposing the lattice, the gas is spin polarized in either the $|F = 9/2, m_F = 9/2\rangle$ or $|F = 9/2, m_F = 7/2\rangle$ state, which we label $|\uparrow\rangle$ and $|\downarrow\rangle$. The atom number and confinement are tuned so that the central density is approximately one atom per site, with the Fermi energy $E_F \approx 7t$. A pair of Raman beams with wavevectors $\vec{k}_1$ and $\vec{k}_2$ intersecting at approximately 30° are focused onto the gas and pulsed to drive spin transitions (Fig. 1). The frequency difference $\Delta\omega = \omega_1 - \omega_2$ between the Raman beams is tuned near to the $|\uparrow\rangle \rightarrow |\downarrow\rangle$ resonance. After a Raman pulse, the number of atoms in each band and spin state is measured using bandmapping with a magnetic field gradient applied during time-of-flight imaging. Atom number loss and heating induced by the Raman pulse are discussed in detail in Appendix A. We observe an approximately 20% atom loss during a (typical) 50 ms pulse due to off-resonant light scattering, which occurs at a relatively high rate because of the limited tuning range of the Raman laser. Heating from the Raman pulse is comparable with that from other sources, and we do not observe atoms excited to higher energy bands.

The Raman beams can drive two resonant processes depending on $\Delta\omega$. If $\Delta\omega$ is tuned to the energy difference between spin states ($\Delta\omega = \omega_{\uparrow\downarrow}$), then on-site spin rotations occur without induced tunneling and changes in site occupancies (Fig. 1a). We define this process as the carrier transition. By tuning the frequency difference between the beams to include U ($\Delta\omega - \omega_{\uparrow\downarrow} = \pm U/\hbar$), density-dependent tunneling is driven as a sideband to the carrier (Fig. 1b). Other processes, such as inter-band transitions, are far off-resonant for the experimental parameters (see Appendix A).

III. CORRELATED SPIN FLIP TUNNELING

To model the dynamics we consider an initially polarized band insulator with driven spin-flip tunneling events. Working in the large U limit, we use perturbation theory

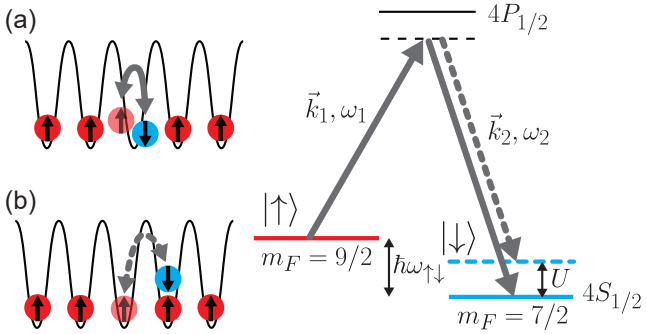

FIG. 1. Schematic diagram of Raman transitions. A pair of Raman beams, each detuned approximately 80 GHz from the $4S_{1/2} \rightarrow 4P_{1/2}$ transition, with frequencies $\omega_{1,2}$ and wavevectors $\vec{k}_{1,2}$ are applied to drive transitions between the $|\uparrow\rangle$ (red) and $|\downarrow\rangle$ (blue) states. The Raman wavevector difference $\delta\vec{k} = \vec{k}_1 - \vec{k}_2$ lies along the $(-1, -1, 1)$ direction of the lattice. Selecting between two distinct processes is achieved by fixing the laser beam frequency ω_1 and tuning ω_2. (a) If the frequency difference matches the Zeeman energy (i.e., $\Delta\omega = \omega_1 - \omega_2 = \omega_{\uparrow\downarrow}$), then atoms flip their spin and remain on the same site. (b) When the laser frequency difference accommodates the Hubbard interaction energy U ($\Delta\omega = \omega_{\uparrow\downarrow} - U/\hbar$), then CSFT occurs and atoms tunnel to neighboring occupied sites and flip their spin. For $|\downarrow\rangle$ as an initial state, the condition for resonant CSFT changes to $\Delta\omega = \omega_{\uparrow\downarrow} + U/\hbar$.

to find the effective Hamiltonian term describing CSFT:

$$H_{\mathrm{CSFT}} = \sum_{i,j \in \mathrm{n.n.}} K_{ij} n_{i\uparrow} (1 - n_{j\downarrow}) c^\dagger_{j\uparrow} c_{i\downarrow} + \mathrm{H.c.} \quad (1)$$

(see Appendix B for derivation). Here, $i, j \in$ n.n. denotes a sum over nearest neighboring sites and permutations, $c^\dagger_{i\sigma}$ ($c_{i\sigma}$) creates (removes) a particle on site i in spin state σ, and $n_{i\sigma}$ is the number of particles on site i in state σ.

CSFT arises as a spin-flip transition to a virtual state offset by U followed by a tunneling event. In contrast to the conventional tunneling term $-tc^\dagger_i c_j$ in the Fermi-Hubbard model, this laser-induced correlated spin-flip tunneling is density dependent and accompanied by a spin rotation. CSFT occurs only when neighboring sites are occupied by atoms in the same spin state or when a doublon (i.e., a $|\uparrow\rangle$–$|\downarrow\rangle$ pair) is next to an empty site. Using a particle-hole transformation, we show (see Appendix B) that Eq. (1) effectively creates singlets to build RVB correlations [25].

The CSFT matrix element is complex and tunable. It is given by (Appendix B):

$$K_{ij} \approx \frac{t\Omega}{2U} \left(e^{-i\delta\vec{k}\cdot\vec{R}_j} - e^{-i\delta\vec{k}\cdot\vec{R}_i} \right), \quad (2)$$

where the ratio $t/U \approx 0.04$–0.08 is controlled by the lattice potential depth s, $\vec{R}_i$ is the location of site i, and $\delta\vec{k}$ is the Raman wavevector difference. For our lattice, $\left|\delta\vec{k} \cdot \left(\vec{R}_i - \vec{R}_j\right)\right| = \pi/2\sqrt{3}$ is the same for every

lattice direction. The Rabi rate for the carrier transition $|\Omega|/\hbar \approx 2\pi \times 650$ Hz is controlled by the Raman laser intensity and measured via Rabi oscillations (Appendix B), and therefore $|K_{ij}|/\hbar \approx 2\pi \times 6$–$22$ Hz for our measurements.

Eq. 1 is the leading order in a large U expansion and has been projected into the subspace connected to the initial spin-polarized $|\uparrow\rangle$ state by resonant CSFT. Other terms can, in principle, contribute to the dynamics. We have verified that the dynamics of the full tight-binding CSFT model (i.e., without the large U approximation) are reproduced by Eq. 1 by applying the time-evolving block decimation algorithm [28] to 1D chains (see Appendix B).

The site-dependent Raman phase in K_{ij} that arises from the Raman wavevector difference is critical to allow tunneling to occur. When spin rotations are driven by long-wavelength radiation or co-propagating Raman beams, this phase factor is absent, and tunneling is prevented. One reason for the absence of tunneling in this scenario can be understood as destructive interference between multiple tunneling pathways caused by the antisymmetrization of the fermionic wavefunctions (see Appendix C). This effect is related to the behavior of clock shifts for fermionic atoms [29–31]. In our case, the Raman phase factor suppresses the destructive tunneling interference.

IV. OBSERVATION OF CORRELATED SPIN FLIP TUNNELING

A. Transfer Fraction Spectroscopy

We spectroscopically resolve CSFT and distinguish it from on-site spin rotations by measuring the change in spin fraction after a 50 ms Raman pulse, which is comparable to the CSFT π-time. Sample data are shown in Fig. 2a for the fraction $f_{\downarrow,\uparrow}$ of atoms transferred between spin states at varied $\Delta\omega$ for $s = 10\ E_R$, where $E_R = \hbar^2/8md^2$ is the recoil energy, m is the atomic mass, and $d \approx 390$ nm is the lattice spacing. Broadening of the carrier transition, which is consistent with contributions from magnetic field and Raman phase noise (see Appendix B), results in a feature that obscures CSFT. To isolate CSFT, we therefore subtract the data taken at identical $\Delta\omega$ with opposite initial spin configurations. Since the carrier frequency does not depend on the initial state, the contribution from the broad carrier feature is canceled out by this procedure. In contrast, the frequency offset of the CSFT sideband changes sign with the initial spin configuration and is not removed by the subtraction. The resulting lineshape for $f_\uparrow - f_\downarrow$ shown in Fig. 2b therefore reveals the CSFT sidebands as peaks offset at approximately $\pm U/\hbar \approx \pm 2\pi \times 3.5$ kHz from the carrier transition.

To compare with the predicted sideband frequency, we fit the $f_\uparrow - f_\downarrow$ lineshape to a sum of two gaussian functions with independent central frequencies and standard deviations as free parameters. The interaction energy U determined from this fit as half of the frequency separation of the peaks is shown in Fig. 2c for data taken at different lattice potential depths. The inferred U increases less rapidly with s than the tight-binding prediction, which is shown as a dashed line. A similar disagreement has been observed in other experiments [32]. The source of this discrepancy is unresolved and cannot be explained by renormalization of U by the Raman process, which is approximately a 1% effect (see Appendix B).

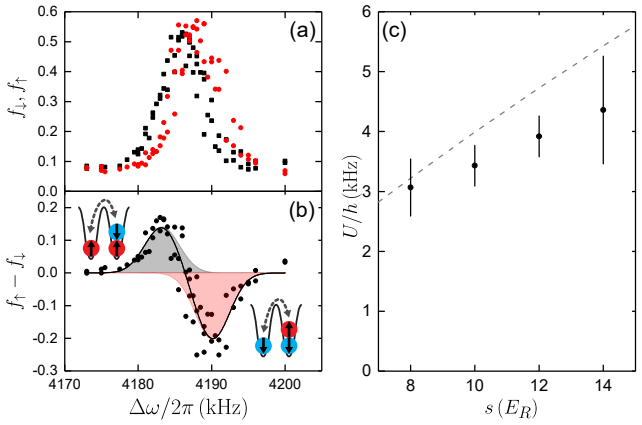

FIG. 2. Spectroscopy of CSFT. (a) The fraction of atoms transferred between spin states by a 50 ms Raman pulse is shown for an initially $|\uparrow\rangle$ (black squares, $f_\uparrow$) and $|\downarrow\rangle$ (red circles, $f_\downarrow$) spin polarized state at $s = 10\ E_R$ for varied $\Delta\omega$. For these measurements, $N = 25400 \pm 3900$ atoms were cooled to $T/T_F = 0.24 \pm 0.08$ before turning on the lattice. Each data point is the result from a single experimental run, and the measurement uncertainty is not visible on this scale. Nonzero transfer at large detuning is due to off-resonant spontaneous Raman scattering. (b) The difference $f_\uparrow - f_\downarrow$ for pairs of points in (a) reveals the CSFT sidebands at approximately $\pm U$. The black line shows a fit to a sum of two gaussian functions; the individual gaussians are displayed as shaded regions. The peak at lower (higher) frequency corresponds to CSFT for an initially $|\uparrow\rangle$ ($|\downarrow\rangle$) spin-polarized state. (c) The interaction energy U inferred from fits to data such as those shown in (b) for varied s. The error bars are derived from the fit uncertainty. The dashed line is the value of U from a standard tight-binding calculation.

B. Double Occupancy Spectroscopy

To isolate CSFT from other dynamics, we measure changes in the doublon number. As doublon formation and decay are strongly suppressed at high interaction strength in the standard Hubbard model [33], doublon generation provides a signature of CSFT dynamics. We probe doublon creation using loss induced by light-assisted collisions (LAC) [34]. The carrier frequency $\omega_{\uparrow\downarrow}$ is estimated using a gaussian fit to Raman

spectroscopy taken using a 0.7 ms pulse, which is too short to drive CSFT. The inset to Fig. 3 shows sample LAC data taken after a 50 ms Raman pulse with $(\Delta\omega - \omega_{\uparrow\downarrow})/2\pi = 3.5$ kHz, which corresponds to the $+U$ CSFT sideband. Immediately following the Raman pulse, the lattice potential depth is rapidly increased to 29 E_R to arrest further dynamics. We measure the number of atoms remaining after a laser pulse 50 MHz detuned from the $4S, F = 9/2 \rightarrow 5P_{3/2}, F = 11/2$ transition is applied to the gas. Two loss processes are evident as the duration τ of the resonant laser pulse is changed. The loss on a fast timescale τ_D corresponds to LAC removing atoms from doubly occupied sites, while the decay over a slower timescale τ_S results from single atoms ejected from the dipole trap via spontaneous scattering. These data are fit to a double exponential decay function $N(\tau) = N_D e^{-\tau/\tau_D} + (N - N_D) e^{-\tau/\tau_S}$ with N, N_D, τ_D and τ_S as free parameters to determine the fraction of doubly occupied sites $D = N_D/N$.

Measurements of D as $\Delta\omega$ is changed show that a resonance for doublon creation is centered near the CSFT spectroscopy sideband peak at $(\Delta\omega - \omega_{\uparrow\downarrow}) \approx U/\hbar$ (Fig. 3). The doublon dynamics near the resonance agree with the rate predicted by H_{CSFT} (see Fig. B3 in Appendix B) and indicate that D has reached a steady state. We therefore compare the data with the fit from Fig. 2b to $|f_\uparrow - f_\downarrow|$, which can be interpreted as the fraction of atoms that flip their spin during CSFT events. The close agreement between the fit and D imply that each spin-flip is associated with the creation of a doublon.

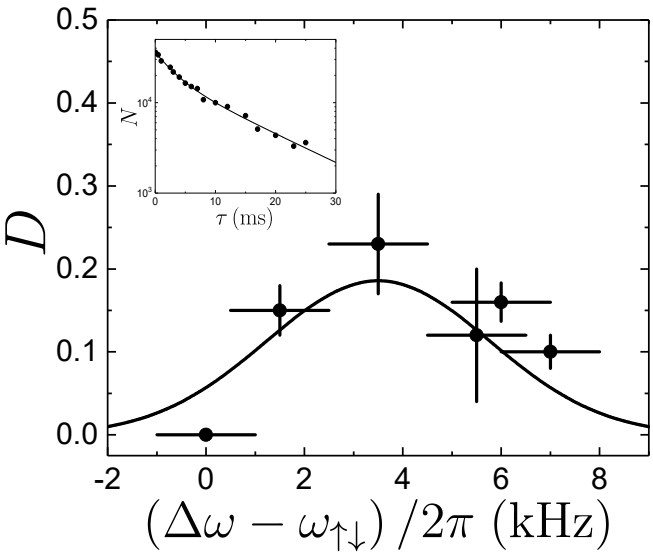

FIG. 3. Fraction of doubly occupied sites D measured after a 50 ms Raman pulse at various detunings for $s = 10$ E_R. The inset shows sample LAC for $(\Delta\omega - \omega_{\uparrow\downarrow})/2\pi = 3.5$ kHz fit to a double-exponential decay with $\tau_D = 3.1 \pm 0.77$ ms and $\tau_S = 13.7 \pm 2.5$ ms. The vertical error bars in D are derived from fits to similar data acquired at different $\Delta\omega$, while the horizontal error bars show the estimated 0.5 kHz uncertainty in the carrier transition from magnetic field drift. The solid line in the main panel is the fit from Fig. 2a for $|f_\uparrow - f_\downarrow|$ plotted on the same scale as D.

C. Vacancy Dependence of Transfer Fraction

Finally, we demonstrate the sensitivity of CSFT to site occupancy by reducing the atom number and controllably introducing vacancies before a Raman pulse on the CSFT sideband (see Fig. 4 inset). Our technique involves three steps. After turning on the lattice to $s = 8$ E_R, atoms are transferred from a spin-polarized initial state (either $|\uparrow\rangle$ or $|\downarrow\rangle$, as in Fig. 2) to the $F = 7/2, m_F = 7/2$ state via adiabatic rapid passage (ARP) driven by a microwave-frequency magnetic field. The power of the microwave field (swept across 0.4 MHz in 0.5 ms) is varied to control the probability of a transition between hyperfine states. The fraction δN of atoms that are not transferred to $F = 7/2$ are removed from the lattice with a 0.5 ms pulse of light resonant with the $4S, F = 9/2 \rightarrow 5P_{3/2}, F = 11/2$ transition. A second ARP sweep (across 0.8 MHz in 1 ms) returns all of the atoms shelved in the $F = 7/2$ manifold to the initial spin state.

After this procedure, unoccupied sites are randomly distributed through the spin-polarized atomic density distribution. The presence of holes suppresses CSFT, which can only occur when adjacent sites are occupied. We probe this effect by measuring changes in $|f_\uparrow - f_\downarrow|$ for a 40 ms Raman pulse with $\Delta\omega$ fixed on the $\pm U$ peaks of the CSFT sideband (Fig. 4). Because the doublon population has saturated (see Fig. B3 in Appendix B), $|f_\uparrow - f_\downarrow|$ coincides with the number of nearest neighbor pairs. As the number of atoms is reduced and the hole density increases, $|f_\uparrow - f_\downarrow|$ decreases, indicating that fewer atoms can participate in CSFT. The data shown in Fig. 4 show good agreement with a prediction of the probability for adjacent sites to be occupied (see Appendix D). For this calculation, the density profile is computed using entropy matching based on s, the overall confinement, and the measured N and T/T_F. The probability of adjacent sites being occupied is determined by averaging over configurations that involve randomly removing a fraction δN of atoms from the simulated density profile.

V. CONCLUSION

We have reported the first observation of density-dependent tunneling in a many-body optical lattice Fermi-Hubbard model. In the future, the spontaneous scattering rate and associated heating and loss can be reduced by a factor of 50 (at constant K) and rendered insignificant by using a laser tuned to an optimal point between the D1 and D2 transitions, which for ^{40}K is at 768.67 nm [35]. Furthermore, reducing the sources of carrier-broadening technical noise by a factor of 3.5 or using a Feshbach resonance to enhance U would enable the CSFT and carrier transitions to be separately resolved.

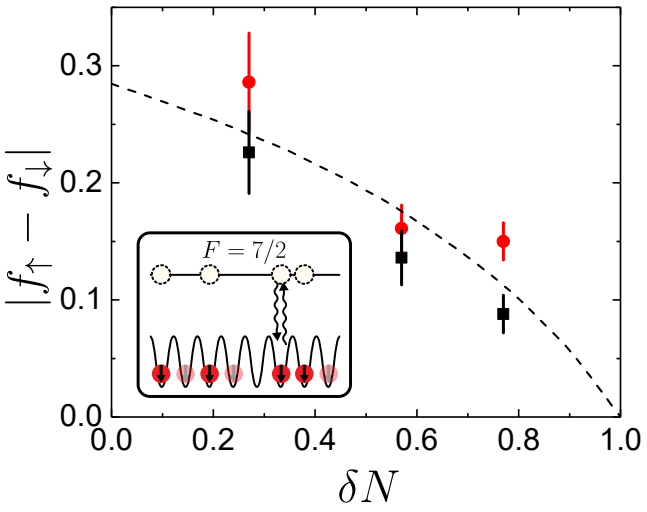

FIG. 4. Density dependence of CSFT. The CSFT spectroscopy signal taken with fixed $(\Delta\omega - \Delta\omega_{\uparrow\downarrow}) \approx \pm U/\hbar$ is shown for varied fraction δN of atoms randomly removed from an $s = 8\ E_R$ lattice gas. For these data, $N = 47000$–81000, and the gas was cooled to $T/T_F \approx 0.35$ before turning on the lattice. Data obtained with the $+U$ sideband are shown as red circles and those for $-U$ as black squares. The sideband frequencies were determined using a double-Gaussian fit to CSFT spectroscopy data, as in Fig. 2b. The dashed line is a prediction for the probability to find adjacent sites occupied based on a calculation of the density profile after the removal procedure. The inset shows the procedure for controllably introducing vacancies. Atoms (shown as transparent) that are not shelved in the $F = 7/2$ state via microwave transitions are removed using resonant light.

The technique we have developed may be used to directly prepare and dynamically evolve RVB order or to observe other exotic states, such as bond-ordered waves, triplet pairing, and hole superconductivity [21]. The site-dependent phase of the bond-charge interaction the Raman lasers introduce also leads to a synthetic gauge field that was not explored in this work. The unique properties of the occupation-dependent gauge field created via this method can be used to simulate interacting relativistic quantum field theories and correlated topological insulators [21].

ACKNOWLEDGMENTS

W.X., W.M., and B.D. acknowledge support from the Army Research Office (W911NF-17-1-0171) and National Science Foundation (PHY 15-05468). V.W.S. and H.H. acknowledge support from the Air Force Office of Scientific Research (FA9550-11-1-0445) and the Army Research Office (W911NF-16-1-0182).

Appendix A: Experimental Sequence and Parameters

Ultracold gases composed of ground-state ^{40}K atoms in the $|F = 9/2, m_F = 9/2\rangle$ and $|F = 9/2, m_F = 7/2\rangle$ states are cooled to temperatures below the Fermi temperature T_F in a crossed-beam 1064 nm optical dipole trap using standard techniques. After evaporative cooling, the optical trap depth is increased to the same value for all the data presented in this paper. The resulting dipole trap frequencies are 7.9 ± 0.4 Hz, 98 ± 1 Hz, and 114 ± 2 Hz. A microwave-frequency swept magnetic field combined with a static magnetic field gradient are used to remove all atoms in one hyperfine state, thereby preparing a spin-polarized gas a with purity of greater than 95% for either spin state. Following spin polarization, we ramp on the three pairs of lattice beams ($\lambda = 782.2$ nm) in 100 ms. The Raman beams are derived from a cavity-stabilized diode laser (Vortex II TLB-6900) and are 80 GHz red-detuned from the $D1$ transition. The frequency and power of each beam are controlled using an acousto-optic modulator.

A 13 G magnetic field is used to lift the degeneracy of Zeeman transitions between different m_F states. The field provides a 27 kHz difference between the $m_F = 9/2 \rightarrow 7/2$ and $m_F = 7/2 \rightarrow 5/2$ transitions. No significant population of $m_F = 5/2$ atoms has been observed in our measurements. The drift in the magnetic field is about 10 mG from day-to-day and 3 mG over the course of a two-hour measurement run.

The magnetic field is reduced to 3 G for imaging. The lattice is ramped down over 100 μs to map band populations onto the momentum distribution [36], and then the dipole trap is turned off for time-of-flight expansion. An additional magnetic field gradient is applied during time-of-flight to spatially separate the two spin components. A gaussian distribution is used to fit the images of each spin component and determine the corresponding atom number.

The minimum band gap (at the band edge) in this work is 31 kHz. For the approximately 10 kHz Raman detunings (from the carrier transition) we sample, the probability for inter-band transitions is therefore negligible. Furthermore, we do not observe excited band population for any of the measurements discussed here.

We observe loss of atoms and heating caused by light scattering from the Raman beams. We characterized this process, which is not fully understood for strongly interacting systems, using measurements at $s = 12\ E_R$. The measured exponential decay constant for N at $s = 12\ E_R$ for Raman-induced loss varied from 130 ± 20 ms to 310 ± 50 ms during the time period when data were acquired. The weighted average of the measured lifetime at $s = 12\ E_R$ was 200 ± 10 ms, which is much longer than the Raman pulses used in this work. Heating is more difficult to measure, given that determining temperature for strongly correlated lattice gases is an outstanding problem. To estimate the heating rate, we measure the tem-

perature in the dipole trap after slowly turning off the lattice. Using this method, we observed a 0.30 ± 0.02 nK/ms heating rate at $s = 12\ E_R$. The measured heating rate without a Raman pulse is 0.13 ± 0.01 nK/ms. We conclude that heating from the Raman pulse is comparable to that from other sources. Furthermore, these data do not show a strong dependence of the heating rate on atom number: the temperature of the gas increases linearly in time, even though the atom number decays (for this measurement) from approximately 2.8×10^4 to 1.7×10^4 over 80 ms.

We also note that the light scattering (and heating and loss rates) could be reduced by a factor of 50 (without changing the Raman Rabi rate) for ^{40}K atoms by using a different laser capable of tuning to 768.67 nm [35]. Moreover, using an atom with a different electronic structure could achieve scattering rates that are many orders of magnitude smaller.

For comparison to theory, U is determined from the lattice depth (as measured by lattice spectroscopy) [37], according to

$$U = \frac{4\pi\hbar^2 a_s}{m} \int |\psi_i(\vec{x})|^4 \, d^3\vec{x}, \tag{A1}$$

where $a_s \approx 174\ a_0$ is the free-space scattering length between the spin states [38], m the atomic mass, and $\psi_i(\vec{x})$ the Wannier wavefunction derived from the tight-binding model. The uncertainty in U is estimated to be less than 2%, and we sample U/t =13–47 in this work.

Appendix B: Theoretical Description of Effective CSFT Hamiltonian

1. Single-Particle Hamiltonian

We first review the Raman-transition Hamiltonian in the absence of interactions and a lattice. Following the standard approach, we consider a three-level system and adiabatically eliminate the intermediate state. This procedure is valid in the $\Omega_{1,2} \ll \Delta_R$ and $\delta \ll \Delta_R$ limits (to be defined subsequently), both of which are well-satisfied in our experiment.

The level diagram for the three-level atom is shown in Fig. B1. The Hamiltonian is

$$H_{3-\mathrm{lev}} = \begin{pmatrix} \omega_{\uparrow\downarrow} & 0 & \frac{\Omega_1^*}{2}\left(e^{-i(\vec{k_1}\cdot\vec{R}-\omega_1 t)} + \text{c.c.}\right) \\ 0 & 0 & \frac{\Omega_2^*}{2}\left(e^{-i(\vec{k_2}\cdot\vec{R}-\omega_2 t)} + \text{c.c.}\right) \\ \frac{\Omega_1}{2}\left(e^{i(\vec{k_1}\cdot\vec{R}-\omega_1 t)} + \text{c.c.}\right) & \frac{\Omega_2}{2}\left(e^{i(\vec{k_2}\cdot\vec{R}-\omega_2 t)} + \text{c.c.}\right) & \omega_0 \end{pmatrix}, \tag{B1}$$

which is written with respect to the $\{|\uparrow\rangle, |\downarrow\rangle, |3\rangle\}$ basis. Here, $\vec{R}$ is the position of the atom, the laser frequencies satisfy $\omega_1 = \omega_0 - \Delta_R - \delta - \omega_{\uparrow\downarrow}$ and $\omega_2 = \omega_0 - \Delta_R$, and the individual Rabi rates $\Omega_{1,2} = -e\left\langle 3 \middle| \vec{E}_{1,2}\cdot\vec{r} \middle| \uparrow,\downarrow \right\rangle$ depend on the dipole matrix elements for the atom–light (with electric field $\vec{E}_i$) interaction.

For the calculations in the main text and discussed in this document, we use a simplified model in which laser beam 1 only couples $|\uparrow\rangle$ and $|3\rangle$, and laser beam 2 only couples $|\downarrow\rangle$ and $|3\rangle$. In the experiment, however, the polarizations of the Raman beams are such that both ground states are coupled to the (multi-level) excited state by both beams. The couplings that we neglect are far from any resonant Raman or single-photon transition and only lead to AC Stark shifts that can be absorbed into the definition of the ground spin states.

We make the rotating-wave approximation and a unitary transformation $H'_{3-\mathrm{lev}} = e^{i\int^t V dt'} H_{3-\mathrm{lev}} e^{-i\int^t V dt'} - V$, with

$$V = \begin{pmatrix} \omega_{\uparrow\downarrow} + \delta & 0 & 0 \\ 0 & 0 & 0 \\ 0 & 0 & \omega_0 - \Delta_R \end{pmatrix}, \tag{B2}$$

which is similar to a transformation to a rotating frame. Projecting $H'_{3-\mathrm{lev}}$ onto the subspace $\{|\uparrow\rangle, |\downarrow\rangle\}$, under the condition $|\Omega_1| \approx |\Omega_2| \ll \Delta_R$, yields

$$H_{2-\mathrm{lev}} \approx \begin{pmatrix} \delta & \frac{\Omega}{2} e^{-i\delta\vec{k}\cdot\vec{R}} \\ \frac{\Omega^*}{2} e^{i\delta\vec{k}\cdot\vec{R}} & 0 \end{pmatrix}, \tag{B3}$$

for an effective Hamiltonian, where $\Omega = -\Omega_1^*\Omega_2/2\Delta_R$ and $\delta\vec{k} = \vec{k_1} - \vec{k_2}$. This projection is equivalent to adiabatically eliminating the excited electronic state. These two levels act as the pseudo-spin basis used in the main part of the text.

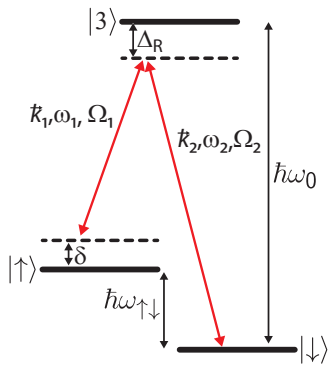

FIG. B1. Energy levels of a 3-level atoms with two lasers of frequencies ω_1 and ω_2.

2. Lattice and Interaction Effects

In the presence of an optical lattice, we project the Hamiltonian onto the lowest Bloch band of the lattice. We denote the Wannier function centered at the site located at $\vec{R}_i$ as $\psi_i(\vec{r}) = \psi\left(\vec{r} - \vec{R}_i\right)$ and $c^\dagger_{i\sigma}$ as the operator that creates a fermion with spin σ at that site. The full tight-binding Hamiltonian is

$$\begin{aligned} H_0 = &- t \sum_{\langle ij\rangle\sigma} \left(c^\dagger_{i\sigma} c_{j\sigma} + \text{hc}\right) \\ &+ \sum_{\langle ij\rangle} \left(\frac{\Omega}{2} e^{-i\delta\vec{k}\cdot\frac{\vec{R}_i+\vec{R}_j}{2}} \Psi_{ij} c^\dagger_{i\uparrow} c_{j\downarrow} + i \leftrightarrow j + \text{hc}\right) \\ &+ \sum_i \left(\frac{\Omega}{2}\Psi_0 e^{-i\delta\vec{k}\cdot\vec{R}_i} c^\dagger_{i\uparrow} c_{i\downarrow} + \frac{\Omega^*}{2}\Psi_0 e^{i\delta\vec{k}\cdot\vec{R}_i} c^\dagger_{i\downarrow} c_{i\uparrow}\right) \\ &+ \frac{\delta}{2}\sum_i \left(n_{i\uparrow} - n_{i\downarrow}\right) + U\sum_i n_{i\uparrow} n_{i\downarrow}, \end{aligned} \tag{B4}$$

where $n_{i\sigma} = c^\dagger_{i\sigma} c_{i\sigma}$, $\Psi_{ij} = \int d\vec{r}\,\psi^*_i e^{i\delta\vec{k}\cdot\left(\vec{R}_i - \vec{R}_j\right)}\psi_j$ is a Debye-Waller factor, $\Psi_0 = \Psi_{00}$, and U is the strength of on-site interaction. The first term is the ordinary spin-conserving tunneling term. The second term is a spin-flip tunneling term akin to spin-orbit coupling in the lattice. The third term is an on-site spin-flip term, which can be understood as an effective Zeeman term in the x, y directions. The fourth term is an effective Zeeman energy. For the experimental parameters explored in this work, we find $\Psi_{ij} \approx \delta_{ij}$. The second term can therefore be safely ignored.

3. Effective Hamiltonian for $\delta \approx U$

To derive an effective Hamiltonian for CSFT, we work in the limit $U, \delta \gg t, \Omega$ and treat the first three terms of H_0 as perturbations. We consider the case $\delta \approx U$ and and project the Hilbert space onto the subspace of states that have the same total Zeeman energy as the initial states. Other states are separated in energy by at least δ and are projected away. The virtual transitions involving these states lead to higher-order (in $1/\delta$) terms in the effective Hamiltonian of the retained states. Off-resonant processes that can take the state out of this subspace (for example, carrier transitions leading to sites occupied by a single spin-down atom) are ignored. This procedure isolates the CSFT dynamics from other aspects of the system. As described in the main text, we also experimentally isolate the CSFT behavior either by studying doublon dynamics or by performing differential spin measurements that remove the carrier contribution. This allows a comparison of only the CSFT portion of the dynamics with theory.

We therefore project our Hamiltonian onto such states where all sites are either empty or occupied by at least a spin-up fermion. Let $\mathcal{P} = \prod_i \left[1 - n_{i\downarrow}(1 - n_{i\uparrow})\right]$ be the projector onto this space. Second-order perturbation theory then gives

$$\begin{aligned} H_{\text{eff}} = \mathcal{P}\Bigg[&-t\sum_{\langle ij\rangle\sigma}\left(c^\dagger_{i\sigma}c_{j\sigma} + \text{hc}\right) - \frac{t\Psi_0}{2}\left(\frac{1}{U} + \frac{1}{\delta}\right)\sum_{\langle ij\rangle}\left(\frac{\Omega^*}{2}\left(e^{i\delta\vec{k}\cdot\vec{R}_i} - e^{i\delta\vec{k}\cdot\vec{R}_j}\right)c^\dagger_{i\downarrow}c_{j\uparrow} + i\leftrightarrow j + \text{hc}\right) \\ &+ \left(\frac{\delta}{2} + \frac{|\Omega|^2\Psi_0^2}{4\delta}\right)\sum_i\left(n_{i\uparrow} - n_{i\downarrow}\right) + U\sum_i n_{i\uparrow}n_{i\downarrow} + \sum_{\langle ij\rangle}\left(\frac{\Omega}{2}e^{-i\delta\vec{k}\cdot\frac{\vec{R}_i+\vec{R}_j}{2}}\Psi_{\text{ij}}c^\dagger_{i\uparrow}c_{j\downarrow} + i\leftrightarrow j + \text{hc}\right) \\ &+ \frac{2t^2}{U}\sum_{\langle ij\rangle}\left(c^\dagger_{i\uparrow}c^\dagger_{i\downarrow}c_{j\downarrow}c_{j\uparrow} + \text{hc}\right) + \frac{2t^2}{U}\sum_{\langle ij\rangle}\left(n_{i\uparrow}n_{i\downarrow}\left(1 - n_{j\uparrow}\right)\left(1 - n_{j\downarrow}\right) + i\leftrightarrow j\right) + \frac{t^2}{U}\sum_{\langle ij\rangle,\langle ij'\rangle,j\neq j'} n_{i\uparrow}c^\dagger_{i\downarrow}c_{j'\downarrow}c^\dagger_{j\downarrow}c_{i\downarrow} \\ &+ \frac{t^2}{U}\sum_{\langle ij\rangle,\langle ij'\rangle,j\neq j'}\left(1 - n_{i\downarrow}\right)c^\dagger_{j\uparrow}c_{i\uparrow}c^\dagger_{i\uparrow}c_{j'\uparrow} - \frac{t^2}{U}\sum_{\langle ij\rangle,\langle ij'\rangle,j\neq j'}\left(c^\dagger_{j\uparrow}c^\dagger_{j'\downarrow}c_{i\uparrow}c_{i\downarrow} + \text{hc}\right)\Bigg]\mathcal{P}. \end{aligned} \tag{B5}$$

Noting that $\Psi_{ij} \approx 0$ for $i \neq j$ and further ignoring higher-order interactions, this can be written as

$$H_{\text{eff}} = \mathcal{P}\left[-t\sum_{\langle ij\rangle\sigma}\left(c^\dagger_{i\sigma}c_{j\sigma}+\text{hc}\right)+\sum_{\langle ij\rangle}\left(K_{ij}c^\dagger_{j\uparrow}c_{i\downarrow}+K_{ji}c^\dagger_{i\uparrow}c_{j\downarrow}+\text{hc}\right)+\frac{\delta^*}{2}\sum_i\left(n_{i\uparrow}-n_{i\downarrow}\right)+U\sum_i n_{i\uparrow}n_{i\downarrow}\right]\mathcal{P}+\mathcal{O}\left(\frac{t^2}{U}\right), \tag{B6}$$

where

$$K_{ij} = -t\Omega\Psi_0\frac{e^{-i\delta\vec{k}\cdot\vec{R}_i}-e^{-i\delta\vec{k}\cdot\vec{R}_j}}{4}\left(\frac{1}{U}+\frac{1}{\delta}\right) \tag{B7}$$

and

$$\delta^* = \delta + \frac{|\Omega\Psi_0|^2}{2\delta}. \tag{B8}$$

H_{eff} governs the dynamics of fully polarized initial states discussed in the main text. The first term moves (but does not create) doublons and holes (e.g., $|\uparrow\downarrow,\downarrow\rangle \to |\downarrow,\uparrow\downarrow\rangle$). The second term is spin-flip tunneling, which due to the projectors $\mathcal{P}$ is effective only if no sites with spin-down are created. We can therefore rewrite the second term by explicitly inserting the projectors: $K_{ij}n_{i\uparrow}(1-n_{j\downarrow})c^\dagger_{j\uparrow}c_{i\downarrow} + i \leftrightarrow j + \text{hc}$. This term can create doublon-hole pairs out of the fully polarized initial state and dominates the dynamics to leading order.

4. Particle–Hole Transformation and Singlet Creation

The effective Hamiltonian (B6) can be recast using a particle-hole transformation into a Hubbard model with singlet creation. We perform the following canonical transformation on Eq. B6:

$$\begin{aligned} c^\dagger_{i\uparrow} &\to \tilde{c}^\dagger_{i\uparrow} \\ c^\dagger_{i\downarrow} &\to (-1)^{P_i}\tilde{c}_{i\downarrow}, \end{aligned} \tag{B9}$$

where, for the bipartite lattices we are considering, $(-1)^{P_i}$ takes on opposite signs for all pairs of nearest neighbors.

This results in a transformed effective Hamiltonian of the form

$$\begin{aligned} \tilde{H}_{\text{eff}} =& \tilde{\mathcal{P}}\left[-t\sum_{\langle ij\rangle}\left(\tilde{c}^\dagger_{i\uparrow}\tilde{c}_{j\uparrow}+\tilde{c}^\dagger_{i\downarrow}\tilde{c}_{j\downarrow}+\text{hc}\right)+\sum_{\langle ij\rangle}\left((-1)^{P_i}K_{ij}\left(\tilde{c}^\dagger_{i\uparrow}\tilde{c}^\dagger_{j\downarrow}-\tilde{c}^\dagger_{i\downarrow}\tilde{c}^\dagger_{j\uparrow}\right)+\text{hc}\right)\right. \\ &\left.+\frac{\delta^*}{2}\sum_i\left(\tilde{n}_{i\uparrow}+\tilde{n}_{i\downarrow}\right)+U\sum_i\tilde{n}_{i\uparrow}(1-\tilde{n}_{i\downarrow})\right]\tilde{\mathcal{P}}+\mathcal{O}\left(\frac{t^2}{U}\right), \end{aligned} \tag{B10}$$

where $\tilde{\mathcal{P}} = \prod_i\left[1-(1-\tilde{n}_{i\downarrow})(1-\tilde{n}_{i\uparrow})\right]$, and $\tilde{n}_{i\sigma} = \tilde{c}^\dagger_{i\sigma}\tilde{c}_{i\sigma}$. In this new basis, the initial state of the system is the fully-occupied state, where each site has two fermions. The projector $\tilde{\mathcal{P}}$ now restricts the Hilbert space to have at least one particle on each site.

Initialized with the fully-filled state, the only effective term in the Hamiltonian (Eq. B10) is the second term, which is of the form $\left(\tilde{c}^\dagger_{i\uparrow}\tilde{c}^\dagger_{j\downarrow}-\tilde{c}^\dagger_{i\downarrow}\tilde{c}^\dagger_{j\uparrow}\right)$. This operator creates a singlet on each pair of nearest-neighbor sites. We can therefore understand the state during the initial stage of the dynamics as a superposition of states consisting of singlet pairs. We also note that the second term effectively implements RVB correlations because the RVB order parameter is $\langle\tilde{c}^\dagger_{i\uparrow}\tilde{c}^\dagger_{j\downarrow}-\tilde{c}^\dagger_{i\downarrow}\tilde{c}^\dagger_{j\uparrow}\rangle$.

The second term in Eq. (B10) creates singlets in time evolution when acting on the initial state. To explain this behavior, we consider a four-site system. The evolution in the early stage can be schematically understood as follows:

$$\begin{aligned} &\left|\widetilde{\uparrow\downarrow},\widetilde{\uparrow\downarrow},\ \widetilde{\uparrow\downarrow},\widetilde{\uparrow\downarrow}\right\rangle \xrightarrow{1-i\tilde{H}_{\text{eff}}\delta t} \text{superposition of} \\ &\qquad\left|\widetilde{\uparrow\downarrow},\widetilde{\uparrow\downarrow},\widetilde{\uparrow\downarrow},\widetilde{\uparrow\downarrow}\right\rangle, \left|\boxed{\tilde{\uparrow},\tilde{\downarrow}},\widetilde{\uparrow\downarrow},\widetilde{\uparrow\downarrow}\right\rangle, \\ &\qquad\left|\widetilde{\uparrow\downarrow},\boxed{\tilde{\uparrow},\tilde{\downarrow}},\widetilde{\uparrow\downarrow}\right\rangle, \left|\widetilde{\uparrow\downarrow},\widetilde{\uparrow\downarrow},\boxed{\tilde{\uparrow},\tilde{\downarrow}}\right\rangle, \end{aligned} \tag{B11}$$

where the outlined sites denote singlet pairs, i.e., $\left|\boxed{\uparrow,\downarrow}\right\rangle \equiv \frac{|\uparrow,\downarrow\rangle-|\downarrow,\uparrow\rangle}{\sqrt{2}}$, and δt is an infinitesimally small time interval such that only the first order effects of $\tilde{H}_{\text{eff}}$ are important. The main dynamics in the early stages of time evolution are therefore the creation of entangled singlet pairs. A comparison between the two bases is tabulated in Table I.

	Original Basis	Transformed Basis
Allowed states of each site	$\|\uparrow\rangle$, $\|\uparrow\downarrow\rangle$,$\|0\rangle$	$\widetilde{\boxed{\uparrow\downarrow}}\rangle$, $\widetilde{\boxed{\uparrow}}\rangle$, $\widetilde{\boxed{\downarrow}}\rangle$
CSFT term	$c^\dagger_{j\uparrow}c_{i\downarrow} - c^\dagger_{i\uparrow}c_{j\downarrow} + \text{hc}$	$\tilde{c}^\dagger_{i\uparrow}\tilde{c}^\dagger_{j\downarrow} - \tilde{c}^\dagger_{i\downarrow}\tilde{c}^\dagger_{j\uparrow} + \text{hc}$
Initial state	$\|\uparrow,\uparrow,\uparrow,\uparrow\rangle$	$\widetilde{\boxed{\uparrow\downarrow}},\widetilde{\uparrow\downarrow},\widetilde{\uparrow\downarrow},\widetilde{\uparrow\downarrow}\rangle$
State after evolution to first order $\left(1 - i\tilde{H}_{\text{eff}}\delta t\right)$	superposition of $\|\uparrow,\uparrow,\uparrow,\uparrow\rangle$, $\left\|\boxed{\uparrow\downarrow, 0},\uparrow,\uparrow\right\rangle$, $\left\|\uparrow,\boxed{\uparrow\downarrow, 0},\uparrow\right\rangle$, $\left\|\uparrow,\uparrow,\boxed{\uparrow\downarrow, 0}\right\rangle$	superposition of $\left\|\widetilde{\uparrow\downarrow},\widetilde{\uparrow\downarrow},\widetilde{\uparrow\downarrow},\widetilde{\uparrow\downarrow}\right\rangle$, $\left\|\boxed{\tilde{\uparrow},\tilde{\downarrow}},\widetilde{\uparrow\downarrow},\widetilde{\uparrow\downarrow}\right\rangle$, $\left\|\widetilde{\uparrow\downarrow},\boxed{\tilde{\uparrow},\tilde{\downarrow}},\widetilde{\uparrow\downarrow}\right\rangle$, $\left\|\widetilde{\uparrow\downarrow},\widetilde{\uparrow\downarrow},\boxed{\tilde{\uparrow},\tilde{\downarrow}}\right\rangle$

TABLE I. Comparison between the original and the transformed basis. In the representation of states, we have used the notation where $\left|\boxed{\uparrow\downarrow, 0}\right\rangle \equiv \frac{|\uparrow\downarrow,0\rangle + |0,\uparrow\downarrow\rangle}{\sqrt{2}}$ and $\left|\boxed{\uparrow,\downarrow}\right\rangle \equiv \frac{|\uparrow,\downarrow\rangle - |\downarrow,\uparrow\rangle}{\sqrt{2}}$.

5. Estimation of U Using the Resonance Near $\delta = U$

The value of the Hubbard U is estimated experimentally via CSFT by finding the resonant δ at which doublon creation is most effective. As discussed in the main text, this procedure appears to undervalue U compared with the tight-binding prediction from independent measurements of the lattice potential depth. To understand how higher-order terms in H_{eff} may explain this discrepancy, we consider a two-site system with the three states $|\uparrow,\uparrow\rangle, |\uparrow\downarrow,0\rangle, |0,\uparrow\downarrow\rangle$ and solve for the value of δ at which the doublon creation rate is maximized. Writing H_{eff} in this basis,

$$\begin{aligned} H^{(2)}_{\text{eff}} &= \begin{pmatrix} \delta + \frac{\Psi_0^2|\Omega|^2}{2\delta} & K_{12} & -K_{21} \\ K_{12}^* & U + \frac{2t^2}{U} & \frac{2t^2}{U} \\ -K_{21}^* & \frac{2t^2}{U} & U + \frac{2t^2}{U} \end{pmatrix} \\ &= \mathcal{U}^\dagger \begin{pmatrix} \delta + \frac{\Psi_0^2|\Omega|^2}{2\delta} & \sqrt{2}K_{12} & 0 \\ \sqrt{2}K_{12}^* & U + \frac{4t^2}{U} & 0 \\ 0 & 0 & U \end{pmatrix} \mathcal{U} \end{aligned} \tag{B12}$$

where $\mathcal{U}$ transforms the basis to $\left\{|\uparrow,\uparrow\rangle, \frac{|\uparrow\downarrow,0\rangle + |0,\uparrow\downarrow\rangle}{\sqrt{2}}, \frac{|\uparrow\downarrow,0\rangle - |0,\uparrow\downarrow\rangle}{\sqrt{2}}\right\}$, and the equality $K_{ij} = -K_{ji}$ has been used. The first two states have the same energy (and hence doublon creation is most effective) when:

$$\delta \approx U + \frac{4t^2 - |\Omega|^2 \Psi_0^2/2}{U} + \frac{2t^2 |\Omega|^2 \Psi_0^2}{U^3} \tag{B13}$$

Here we see that the resonant condition for maximal doublon creation is not exactly at $\delta = U$, but instead shows higher-order corrections. These corrections contribute to the deviation between the measured and predicted U discussed in the main text. However, the predicted 1% deviation is too small to explain the observed discrepancy.

6. Validating the CSFT Effective Hamiltonian

The effective model H_{eff} is a perturbative result, in comparison to the full tight-binding Hamiltonian H_0. To test the validity of the doublon dynamics predicted by H_{eff}, we compare the time evolution of the doublon population in both models. This allows us to benchmark the effective Hamiltonian against an exact numerical simulation.

The dynamics of H_0 cannot be solved exactly in large systems with dimension higher than one. We therefore consider doublon dynamics in one-dimension. We initialize a one-dimensional infinite system with one spin-up fermion in each state, and evolve it with infinite time-evolving block decimation (iTEBD) [28]. The evolution of doublon fraction, defined as $D = \langle n_{i\uparrow} n_{i\downarrow}\rangle / \langle n_{i\uparrow} + n_{i\downarrow}\rangle$, is plotted in Fig. B2(a). The simulations performed with H_0 and H_{eff} are both presented.

Here we see that the effective model captures the qualitative features of the full Hamiltonian. The doublon creation rate at short times is essentially the same for both models. Furthermore, the long-time steady-state reveals approximately the same doublon fraction. In both models the timescale of equilibration is roughly set by $\hbar/|K_{\langle ij\rangle}| = 14$ms. We therefore see that the effective CSFT model H_{eff} captures the essential features of the full tight-binding model H_0 in one dimension.

7. CSFT Timescale: Theory–Experiment Comparison

We measure the Rabi rate of the carrier $\Psi_0 |\Omega| / \hbar = 2\pi \times 650$ Hz using resonant Rabi oscillations. The carrier frequency $\omega_{\uparrow\downarrow}$ is determined using a fit of the spin transition probability vs. Raman detuning $\Delta\omega$ for a 0.7 ms pulse, which is too short to drive CSFT.

Measuring the slower rate for CSFT requires a longer timescale. We eliminate the background contribution from the broadened carrier feature using the same pro-

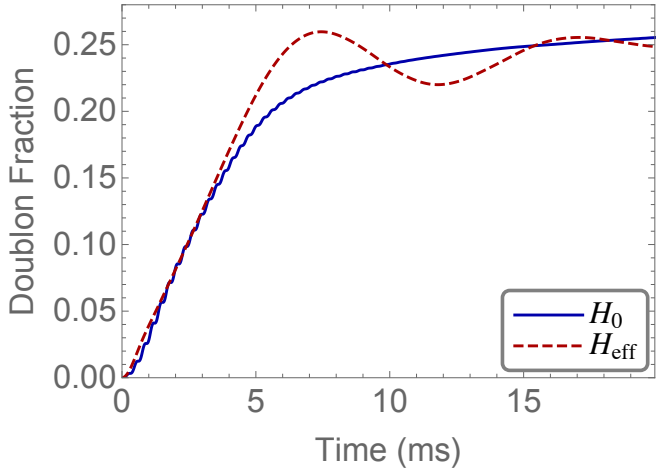

FIG. B2. The evolution of doublon fraction $\langle n_{i\uparrow}n_{i\downarrow}\rangle/\langle n_{i\uparrow}+n_{i\downarrow}\rangle$ from a numerical simulation with constant Ω. The solid lines shows the simulation with the full Hamiltonian H_0, while the dashed line shows that with the effective Hamiltonian H_{eff} derived from second-order perturbation theory. The states are initialized with one spin-up fermion on every site, and the parameters are determined by experiment: $t/h = 0.25$kHz, $U/h = 3.22$kHz, $\Omega = 0.1U$ and $\delta\vec{k}\cdot\vec{d} = \pi/2\sqrt{3}$, where $\vec{d}$ is a lattice vector.

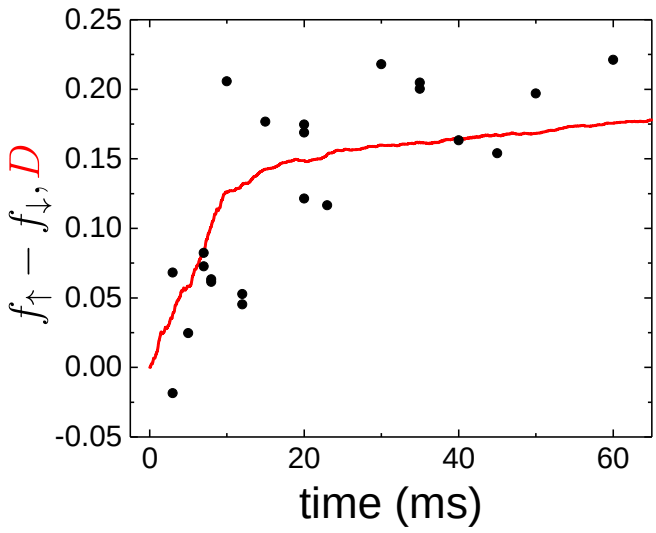

FIG. B3. CSFT signal for varied Raman pulse time. The Raman detuning for these measurements is fixed to the $+U$ CSFT sideband. The measurements are shown using black circles, and a theoretical simulation is displayed as a red line. The simulation is performed with Ω in H_0 replaced with $\Omega e^{i\phi(t)}$, where $\langle\langle\phi(t)^2\rangle\rangle$=8, and the characteristic timescale of the fluctuations in $\phi(t)$ is 2 ms. The dynamics has been averaged (indicated by the notation $\langle\langle\rangle\rangle$) over five realizations of $\phi(t)$. For these parameters, the carrier Rabi oscillations are not strongly perturbed.

cedure as for Fig. 4 in the main text. After locating the carrier frequency $\omega_{\uparrow\downarrow}$, we perform two measurements with the same Raman pulse time at $\Delta\omega = \omega_{\uparrow\downarrow} + U/\hbar$, but with different initial spin polarization. The difference between these two measurements $f_\uparrow - f_\downarrow$ reflects only the CSFT process. Fig. B3 shows the measured CSFT signal for different Raman pulse times at $s = 8\ E_R$ lattice depth.

The measured CSFT timescale is approximately a factor of five larger than that of the numerical simulations shown in Fig. B2, which use the experimentally determined carrier Rabi rate. The uncertainty in t and U (which determine K_{ij} and the CSFT timescale) from measurements of the lattice potential depth are too small to support this difference.

A potential source of this discrepancy is phase-noise between the Raman laser beams, which translates into fluctuations in the complex phase of Ω in H_{eff}. Such noise can arise from, for example, differential acoustic vibrations of the opto-mechanics or fibers in the physically distinct and spatially separated Raman beam paths or the separate optical power servos we use for each beam. Phase noise with a non-uniform frequency spectrum is required to explain the inconsistency we observe, since the predicted CSFT time dependence shown in Fig. B2 is constrained by all the experimental parameters, including the independent measurement of $|\Omega|$ using the carrier transition. In order to differentially affect the carrier and CSFT transitions, the phase-noise spectral density must be frequency dependent.

To explore this, we carry out iTEBD numerical simulations with a time-dependent $\Omega e^{i\phi(t)}$. The result, plotted as the solid line in Fig. B3, shows better agreement with the experimental result. The noise we introduce in this simulation is generally consistent with experimental sources of phase instability between the Raman beams. This phase noise may also explain the broadening of the CSFT peaks evident in Fig. 2 in the main text. We reserve a detailed discussion of the noise and comparison with experiment to future work [39].

Appendix C: Raman Phase Gradient and Fermionic Statistics

As discussed in the main text, the spatially dependent Raman phase that arises because the Raman beams intersect at an angle plays a key role in enabling CSFT. We use a two-site, two-atom toy model to explain how the Raman phase disrupts destructive interference between multiple tunneling pathways that is induced by antisymmetrization of the wavefunction.

Considering a two-site, two-fermion system, there are six possible configurations, which we label according to the site and spin occupancy in each well: $|\uparrow,\uparrow\rangle_W$, $|\downarrow,\downarrow\rangle_W$, $|\uparrow\downarrow,0\rangle_W$, $|0,\uparrow\downarrow\rangle_W$, $|\uparrow,\downarrow\rangle_W$, and $|\downarrow,\uparrow\rangle_W$. In this well-specific basis, $|\downarrow,\uparrow\rangle_W$ means that a $|\downarrow\rangle$ atom is in the left well (located at position $\vec{R}_1$) and an $|\uparrow\rangle$ atom is in the right well (located at position $\vec{R}_2$), for example.

Using a Slater determinant to explicitly write down

properly symmetrized (un-normalized) two-atom wavefunctions, we have:

$$|\uparrow,\uparrow\rangle_W = (|LR\rangle - |RL\rangle)\,|\uparrow\uparrow\rangle \tag{C1}$$
$$|\downarrow,\downarrow\rangle_W = (|LR\rangle - |RL\rangle)\,|\downarrow\downarrow\rangle \tag{C2}$$
$$|\downarrow\uparrow,0\rangle_W = |LL\rangle\,(|\uparrow\downarrow\rangle - |\uparrow\downarrow\rangle) \tag{C3}$$
$$|0,\downarrow\uparrow\rangle_W = |RR\rangle\,(|\uparrow\downarrow\rangle - |\uparrow\downarrow\rangle) \tag{C4}$$
$$|\uparrow,\downarrow\rangle_W = (|LR\rangle - |RL\rangle)(|\uparrow\downarrow\rangle + |\downarrow\uparrow\rangle) + (|LR\rangle + |RL\rangle)(|\uparrow\downarrow\rangle - |\downarrow\uparrow\rangle) \tag{C5}$$
$$|\downarrow,\uparrow\rangle_W = (|LR\rangle - |RL\rangle)(|\uparrow\downarrow\rangle + |\downarrow\uparrow\rangle) - (|LR\rangle + |RL\rangle)(|\uparrow\downarrow\rangle - |\downarrow\uparrow\rangle), \tag{C6}$$

where the spatial part of the wavefunction is written in the basis of $|L\rangle$ and $|R\rangle$, which are single-particle states on either the left or the right well, and the spin component is denoted as $|\uparrow\rangle$ and $|\downarrow\rangle$. For example, in this basis, $|LR\rangle\,|\uparrow\downarrow\rangle$ means that atom 1 is in the left well in the $|\uparrow\rangle$ state, and atom 2 is in the right well in the $|\downarrow\rangle$ state. The key point for this discussion is that the $|\uparrow,\downarrow\rangle_W$ and $|\downarrow,\uparrow\rangle_W$ states consist of spin singlet and triplet components. Furthermore, the relative sign between the spin and triplet components is opposite for these two states.

We focus on resonant CSFT with $\Delta\omega = U/\hbar$. An initially spin-polarized state $|\uparrow,\uparrow\rangle_W$ (as in the experiment) can transition to a virtual state $|\uparrow,\downarrow\rangle_W$ or $|\downarrow,\uparrow\rangle_W$ via a Raman transition (see Fig. C1). The amplitude for this process is suppressed by a factor of $1/U$ because of the energy mismatch. The phase of the virtual state depends on which atom undergoes a spin-flip, since $\delta\vec{k} \neq 0$. Therefore, the Raman phase enters as either $e^{\delta\vec{k}\cdot\vec{R}_1}$ or $e^{\delta\vec{k}\cdot\vec{R}_2}$, where $\vec{R}_1$ and $\vec{R}_2$ differ by a lattice vector $\vec{d}$. After the virtual state is formed, tunneling completes the CSFT process, and a doublon is formed. Via tunneling, the sign difference between equations C5 and C6 is converted into an overall sign difference between the wavefunctions for each doublon-formation pathway. This π relative phase between the wavefunctions can be computed from the tunneling matrix elements $\langle\uparrow\downarrow,0|_W\, t(c_i^\dagger c_{i+1}+\text{h.c.})\,|\uparrow,\downarrow\rangle_W$ and $\langle\uparrow\downarrow,0|_W\, t(c_i^\dagger c_{i+1}+\text{h.c.})\,|\downarrow,\uparrow\rangle_W$.

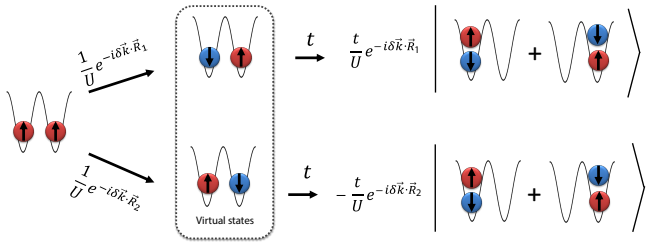

FIG. C1. A schematic diagram showing CSFT for a two-site two-fermion system. CSFT happens as a two-step process via a virtual state. Two possible channels between the initial state $|\uparrow,\uparrow\rangle_W$ and the final state $|\uparrow\downarrow,0\rangle_W + |0,\uparrow\downarrow\rangle_W$ happen simultaneously but with amplitudes carrying opposite signs. The probability to observe a doublon-hole pair is affected by interference between these channels.

The transition between the between the initial state $|\uparrow,\uparrow\rangle_W$ and the final doublon–hole state happens via these two possible channels simultaneously. The final state is a superposition of these two pathways, with a wavefunction proportional to $\left(e^{-i\delta\vec{k}\cdot\vec{R}_1} - e^{-i\delta\vec{k}\cdot\vec{R}_2}\right)(|\uparrow\downarrow,0\rangle + |0,\uparrow\downarrow\rangle)$. The probability to observe a doublon-hole state is thus proportional to $[1- -\cos(\delta\vec{k}\cdot\vec{d})\Big]$. Without the Raman phase gradient (i.e., $\delta\vec{k} = 0$ or $\delta\vec{k}\cdot\vec{d} = 0$), destructive interference prevents tunneling, and doublons will not be formed. Ultimately, this interference arises from the different signs between the triplet and singlet components in equations C5 and C6—it is absent for bosons, for instance.

Appendix D: Simulation of CSFT Sensitivity to Vacancies

We developed a simple numerical simulation (shown in Fig. 4 in the main text) to determine the sensitivity of CSFT to vacancies in the lattice. We compute a density distribution in the non-interacting limit, and determine the probability that neighboring sites are occupied as atoms are randomly removed. The density distribution after turning on the lattice is generated according to $n\,(r_x, r_y, r_z) = \int \frac{d^3\vec{q}}{h^3} \frac{1}{e^{\beta[V(r_x,r_y,r_z)+\epsilon(\vec{q})-\mu]}+1}$, where $V\,(r_x, r_y, r_z)$ is the total harmonic potential imposed by optical trap and lattice beams, μ is the chemical potential, $\beta = 1/k_B\tilde{T}$, $\epsilon\,(\vec{q}) = 2t\,(3 - \cos\pi q_x/q_B - \cos\pi q_y/q_B - \cos\pi q_z/q_B)$ is the lattice dispersion, $q_B = \hbar\pi/d$, and $\tilde{T}$ the effective temperature in the lattice. Both μ and $\tilde{T}$ are solved by matching the entropy and number of atoms N to the corresponding values in the dipole trap. Non-interacting thermodynamics (including the tight-binding lattice dispersion and confining potential) are solved to relate the entropy to N and $\tilde{T}$. Each site in the simulated lattice is computed as occupied by a single atom or empty based on comparing a random number in the interval $[0, 1]$ to $n\,(r_x, r_y, r_z)$.

Atoms are randomly removed from the simulated density profile according to a probability δN, which corre-

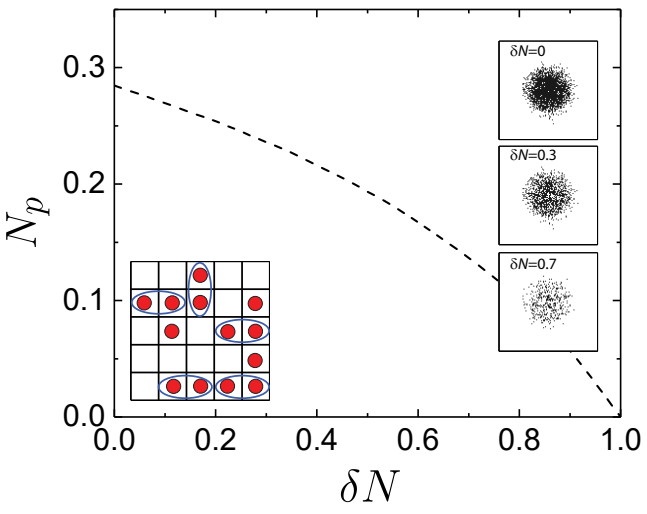

FIG. D1. The fraction of atoms with nearest neighbors at various removal fractions δN for $N = 61000$ and $S/N = 2.89\ k_B$, which corresponds to $k_B\tilde{T} = 9.7t$ and chemical potential $\mu = 6.4t$ in the lattice. The insets at the right show sample occupation profiles (with one black dot per atom) through a central slice of the gas. The inset at bottom left schematically illustrates the procedure for counting pairs.

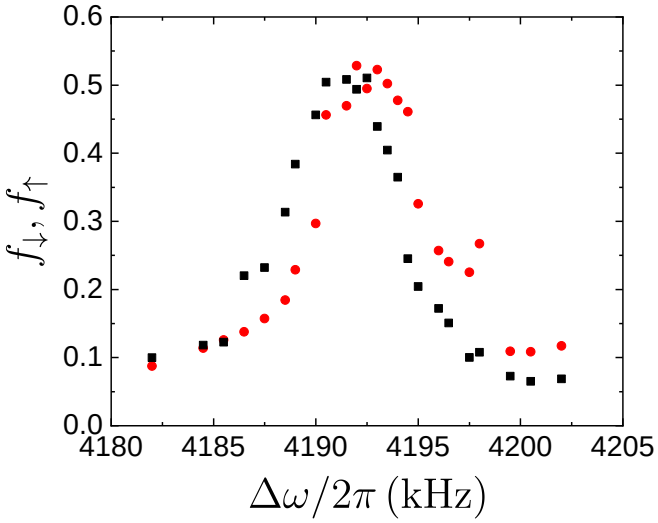

FIG. D2. Measurements of $f_\uparrow$ (black squares) and $f_\downarrow$ (red circles) for varied Raman detuning $\Delta\omega$ taken using the same procedure as for Fig. 2 in the main text. For these data, $\delta N \approx 0.57$.

sponds to the average fraction of atoms discarded. The fraction N_p of atoms in adjacent occupied sites remaining after this removal procedure is counted. As shown in an inset to Fig. D1, atoms are only counted once if they participate in any nearest-neighbor pair. Results from this simulation for the fraction of atoms N_p are shown in Fig. D1 for $N = 61000$ and entropy per particle $S/N = 2.89k_B$ in the lattice. This curve is plotted in Fig. 4 in the main text.

Our simulation includes the Raman-induced atom loss in δN. For the measurements in Fig. 4 in the main text, the initial conditions before the controlled removal procedure are $N = 80900 \pm 3940, T/T_F = 0.29 \pm 0.04$; $N = 54800 \pm 12500$, $T/T_F = 0.34 \pm 0.04$; and $N = 47200 \pm 2810$, $T/T_F = 0.38 \pm 0.08$ from high to low δN. After removal and loss induced by the Raman beams, the atom number is 59200 ± 2660, 23700 ± 1830, and 10900 ± 5180, from high to low δN.

The procedure described in the main text for determining how D depends on δN involves measurements of $f_\uparrow$ and $f_\downarrow$. We observe that the CSFT spectrum is not altered qualitatively by changes in N for the range of δN sampled in Fig. 4 in the main text. Sample data are shown in Fig. D2 for $\delta N \approx 0.57$.

[1] A. Eckardt, Rev. Mod. Phys. **89**, 011004 (2017).
[2] C. V. Parker, L.-C. Ha, and C. Chin, Nat. Phys. **9**, 769 (2013).
[3] J. Struck, C. Ölschläger, R. Le Targat, P. Soltan-Panahi, A. Eckardt, M. Lewenstein, P. Windpassinger, and K. Sengstock, Science **333**, 996 (2011).
[4] Y.-J. Lin, R. L. Compton, A. R. Perry, W. D. Phillips, J. V. Porto, and I. B. Spielman, Phys. Rev. Lett. **102**, 130401 (2009).
[5] M. Aidelsburger, M. Atala, M. Lohse, J. T. Barreiro, B. Paredes, and I. Bloch, Phys. Rev. Lett. **111**, 185301 (2013).
[6] H. Miyake, G. A. Siviloglou, C. J. Kennedy, W. C. Burton, and W. Ketterle, Phys. Rev. Lett. **111**, 185302 (2013).
[7] J. Struck, C. Ölschläger, M. Weinberg, P. Hauke, J. Simonet, A. Eckardt, M. Lewenstein, K. Sengstock, and P. Windpassinger, Phys. Rev. Lett. **108**, 225304 (2012).
[8] G. Jotzu, M. Messer, R. Desbuquois, M. Lebrat, T. Uehlinger, D. Greif, and T. Esslinger, Nature **515**, 237 (2014).
[9] J. Hirsch, Physica C **158**, 326 (1989).
[10] W. P. Su, J. R. Schrieffer, and A. J. Heeger, Phys. Rev. Lett. **42**, 1698 (1979).
[11] D. K. Campbell, J. T. Gammel, and E. Y. Loh, Phys. Rev. B **42**, 475 (1990).
[12] W. G. Van der Wiel, S. De Franceschi, J. M. Elzerman, T. Fujisawa, S. Tarucha, and L. P. Kouwenhoven, Rev. Mod. Phys. **75** (2002).
[13] S. Greschner, G. Sun, D. Poletti, and L. Santos, Phys. Rev. Lett. **113**, 215303 (2014).
[14] Á. Rapp, X. Deng, and L. Santos, Phys. Rev. Lett. **109**, 203005 (2012).
[15] S. Greschner and L. Santos, Phys. Rev. Lett. **115**, 053002 (2015).
[16] S. Fölling, S. Trotzky, P. Cheinet, M. Feld, R. Saers, A. Widera, T. Müller, and I. Bloch, Nature **448**, 1029 (2007).
[17] Y.-A. Chen, S. Nascimbène, M. Aidelsburger, M. Atala, S. Trotzky, and I. Bloch, Phys. Rev. Lett. **107**, 210405 (2011).
[18] R. Desbuquois, M. Messer, F. Görg, K. Sandholzer, G. Jotzu, and T. Esslinger, Phys. Rev. A **96**, 053602 (2017).
[19] R. Ma, M. E. Tai, P. M. Preiss, W. S. Bakr, J. Simon, and M. Greiner, Phys. Rev. Lett. **107**, 095301 (2011).
[20] F. Meinert, M. J. Mark, K. Lauber, A. J. Daley, and H.-C. Nägerl, Phys. Rev. Lett. **116**, 205301 (2016).
[21] A. Bermudez and D. Porras, New J. Phys **17**, 103021 (2015).
[22] M. D. Liberto, C. E. Creffield, G. I. Japaridze, and C. M. Smith, Phys. Rev. A **89**, 013624 (2014).
[23] M. Troyer and U.-J. Wiese, Phys. Rev. Lett. **94**, 170201 (2005).
[24] P. Anderson, Science **235**, 1196 (1987).
[25] G. Baskaran, Z. Zou, and P. Anderson, Solid State Commun. **88**, 853 (1993).
[26] S. Nascimbène, Y.-A. Chen, M. Atala, M. Aidelsburger, S. Trotzky, B. Paredes, and I. Bloch, Phys. Rev. Lett. **108**, 205301 (2012).
[27] D. McKay and B. DeMarco, Rep. Prog. Phys. **74**, 054401 (2011).
[28] G. Vidal, Phys. Rev. Lett. **98**, 070201 (2007).
[29] S. Gupta, Z. Hadzibabic, M. Zwierlein, C. Stan, K. Dieckmann, C. Schunck, E. Van Kempen, B. Verhaar, and W. Ketterle, Science **300**, 1723 (2003).
[30] A. M. Rey, A. V. Gorshkov, and C. Rubbo, Phys. Rev. Lett. **103**, 260402 (2009).
[31] E. L. Hazlett, Y. Zhang, R. W. Stites, K. Gibble, and K. M. O'Hara, Phys. Rev. Lett. **110**, 160801 (2013).
[32] R. Jördens, N. Strohmaier, K. Günter, H. Moritz, and T. Esslinger, Nature **455**, 204 (2008).
[33] N. Strohmaier, D. Greif, R. Jördens, L. Tarruell, H. Moritz, T. Esslinger, R. Sensarma, D. Pekker, E. Altman, and E. Demler, Phys. Rev. Lett. **104**, 080401 (2010).
[34] M. T. DePue, C. McCormick, S. L. Winoto, S. Oliver, and D. S. Weiss, Phys. Rev. Lett. **82**, 2262 (1999).
[35] R. Ozeri, W. M. Itano, R. B. Blakestad, J. Britton, J. Chiaverini, J. D. Jost, C. Langer, D. Leibfried, R. Reichle, S. Seidelin, J. H. Wesenberg, and D. J. Wineland, Phys. Rev. A **75**, 042329 (2007).
[36] D. McKay, M. White, and B. DeMarco, Phys. Rev. A **79**, 063605 (2009).
[37] D. Jaksch, C. Bruder, J. I. Cirac, C. W. Gardiner, and P. Zoller, Phys. Rev. Lett. **81**, 3108 (1998).
[38] S. Falke, H. Knöckel, J. Friebe, M. Riedmann, E. Tiemann, and C. Lisdat, Phys. Rev. A **78**, 012503 (2008).
[39] H.-Y. Hui, W. Xu, W. Morong, B. DeMarco, and V. Scarola, Unpublished.